Supporting Information

The electronic structure of the novel [4Fe-3S] cluster in O2-tolerant hydrogenases characterized by ^{57}Fe Mössbauer and EPR spectroscopy.

Maria-Eirini Pandelia*, Dmytro Bykov, Robert Izsak, Pascale Infossi, Marie-Thérèse Giudici-Orticoni, Eckhard Bill*, Frank Neese, and Wolfgang Lubitz*

Materials and Methods

Sample purification and preparation. The hyperthermophilic bacterium *A. aeolicus* was grown at 85°C in two-liter bottles under a $CO_2/H_2/O_2$ atmosphere . Hydrogenase I was purified at room temperature under semi-anaerobic conditions in a 50 mM Tris-HCl buffer pH 7.0, in the presence of 5-10 % glycerol and 0.01 % n-dodecyl-β-D-maltoside (DDM) as previously described (1). The enzyme used for Mössbauer measurements was enriched using ^{57}Fe (metallic ^{57}Fe (~95%) purchased from Chemotrade, Düsseldorf), following the growth and purification protocol described above for the non-labeled case.

Super-Oxidation with porphyrexide ($C_5H_9N_4$). The porphyrexide (4-amino-2 imino-5,5-dimethyl-2,5-dihydro-1*H*-imidazole-1-oxyl) was synthesized in-house by oxidizing 2,4-Diamino-5,5-dimethyl-5*H*-imidazole 1-oxide (Sigma Aldrich). The purity of the compound was confirmed by IR spectroscopy and its midpoint potential was determined to be E_m = +698 mV (quoted relative to standard hydrogen electrode) in H_2O by cyclic voltammetry (CV), which is very close to that reported elsewhere (2). The porphyrexide solution was freshly prepared in pure water on ice as it was found that it reacts with the Hepes/Tris buffers (most likely can oxidize them). A 10 times excess of porphyrexide was shown to be adequate to super-oxidize the hydrogenase sample from *A. aeolicus* ([3Fe4S] uncoupled signal was of the order of 5% or less), since part of it reacted most likely with the buffer itself (aerobic addition, total reaction time 10 minutes).

Super-Oxidation with air. Samples which are prepared in normal atmosphere as described above are to ca. 80% in the super-oxidized state, i.e the [NiFe] site, and the medial and distal FeS clusters are oxidized in their $[3Fe\text{-}4S]^{1+}$, and $[4Fe\text{-}4S]^{2+}$ states, respectively, whereas the proximal cluster is ca. 80% in $[4Fe\text{-}3S]^{5+}$ state, and 20% in $[4Fe\text{-}3S]^{4+}$ state. The oxidation states, which have been estimated from redox potentials (3) , have been verified by EPR measurements on aliquots of the Mössbauer samples and by simulations of the Mössbauer spectra. In the main manuscript, the spectra of the aerobically isolated sample are shown (Fig. 3B) accounting for 80% of the proximal iron-sulfur clusters in the super-oxidized state. The spectra of the porphyrexide oxidized sample were fitted considering 100% of the proximal iron-sulfur clusters and could be fitted with the same parameters. However, due to extensive degradation of the samples due to the very oxidative treatment, the spectra of the aerobically oxidized sample are shown in the main manuscript.

Partial reduction with sodium ascorbate. The sodium ascorbate (Sigma-Aldrich) has been added to the sample prior treated with porphyrexide. As the porphyrexide could not be removed even after dialysis of the sample, an excess of sodium ascorbate was used to reduce the sample and set the potential in the solution to +130 ± 20 mV (pH 7.25) (3). The excess of sodium ascorbate used (20 times excess relative the sample concentration), was partially consumed by the porphyrexide present in the solution.

Reduction with hydrogen. Hase I was reduced with hydrated dihydrogen (N27, Air Liquide) for two hours in an anaerobic glovebox (Coy) to ensure full reduction of all the iron-sulfur cofactors. Full reduction of all the FeS clusters was subsequently determined and quantified by EPR spectroscopy.

UV-visible spectroscopy. Optical spectra were recorded in a Shimadzu UV-2401 PC spectrometer, controlled by UVPC software Version 3.9. All measurements were performed in quartz cuvettes with 1 cm optical path length at room temperature.

EPR spectroscopy. Continuous wave (cw) X-Band measurements were carried out using an X-band Bruker ESP 300E spectrometer (9.4 GHz, TE_{102} resonator) equipped with an Oxford Instruments helium flow cryostat (Oxford Instr., ESR910) and an ITC 503 temperature controller. cw and pulsed W-band measurements were carried out in a Bruker Elexsys E-680 FT EPR W-band spectrometer with a helium flow cryostat and a variable-temperature TeraFlex Bruker resonator. EPR spectra were obtained by integration over the two-pulse echo sequence ($\pi/2$-τ-$\pi/2$). Typical $\pi/2$ lengths were 12-20 ns.

Mössbauer Spectroscopy. Mössbauer spectra were recorded on a conventional spectrometer with alternating constant acceleration of the source. The minimum experimental line width was 0.24 $mm \cdot s^{-1}$ (full-width at half maximum). The sample temperature was maintained constant either in an Oxford Variox or an Oxford Mössbauer-Spectromag cryostat. The latter is a split-pair conducting magnet system for applying fields of up to 8 T to the samples that can be kept at temperatures in the range 1.5–250 K. The field at the sample is perpendicular to the γ-beam. All isomer shifts are quoted relative to iron metal at 300 K.

EPR spectra simulation. The absorption and derivative EPR spectra were simulated using the MATLAB (Mathworks) based *EasySpin* simulation software by taking into account *A*- and *g*-strain effects contributing to the inhomogeneous linewidth of the EPR lines (4). The spin Hamiltonian for an exchange-coupled three-spin system was taken as (5):

$$\hat{H} = -\sum_{\substack{i=1:3 \\ j>i}} 2J_{ij}\hat{\vec{S}}_i \cdot \hat{\vec{S}}_j + \sum_{\substack{i=1:3 \\ j>i}} 2\hat{\vec{S}}_i \cdot \tilde{d}_{ij} \cdot \hat{\vec{S}}_j + \sum_{i=1:3} \mu_B \vec{B}_0 \cdot \tilde{g}_i \cdot \hat{\vec{S}}_i, \qquad \text{(Eq. 1)}$$

where the first term is the Heisenberg exchange. The second term in Eq. 3 is the magnetic dipolar coupling. Dipolar coupling mainly depends on the distance between paramagnetic centers. Using the point-dipole approximation the tensor $\mathbf{d_{ij}}$ can be expressed as:

$$\tilde{d}_{ij} = \frac{\mu_B^2}{r_{ij}^3}\left(\tilde{g}_i \cdot \tilde{g}_j - \frac{3(\tilde{g}_i\vec{r}_{ij}) \cdot (\tilde{g}_j\vec{r}_{ij})}{r_{ij}^2}\right), \qquad \text{(Eq. 2)}$$

where r_{ij} is the distance vector between two paramagnetic centers and g_i and g_j are the *g*-matrices of the respective centers (considered to be anisotropic). A more accurate description would require exact knowledge of the projection factors of the dipolar interaction between each Fe ion. In this article, we consider only the isotropic part of the exchange coupling tensor *J*, because the anisotropic part is typically small and it would require an overparametrization of the defined system (3 interacting $S = 1/2$ spins with anisotropic *g*-tensors, one of which is unknown). The last term of Eq. 1 contains the electronic Zeeman interaction.

Mössbauer Simulations. The zero-magnetic field spectra were simulated by using symmetric quadrupole doublets with Lorentzian line shapes. H_2-reduced enzyme: The subcomponents have been fitted with similar line widths (0.30 - 0.37 mm s^{-1}). Only a quadrupole doublet accounting for a single Fe site having an unusually large quadrupole coupling ($|\Delta E_Q|$ = 2.61 mm s^{-1}) was fitted with 0.26 mm s^{-1}. Ascorbate reduced enzyme: The subcomponents have been fitted with similar line widths (0.30 - 0.32 mm s^{-1}). Only a quadrupole doublet accounting for a single Fe site having an unusually large quadrupole coupling ($|\Delta E_Q|$ = 2.23 mm s^{-1}) was fitted with 0.36 mm s^{-1} Porphyrexide oxidized enzyme: The subcomponents have been fitted with similar line widths 0.30-0.35 mm s^{-1}. Only a quadrupole doublet accounting for a single Fe site having an unusually large quadrupole coupling ($|\Delta E_Q|$ = 2.42 mm s^{-1}) was fitted with 0.26 mm s^{-1} line width.
Magnetic Mössbauer spectra of the reduced samples were simulated by superposition of spectra calculated for independent paramagnetic clusters with strong intrinsic spin coupling and without inter-cluster coupling. The electronic spin Hamiltonians to this end comprised the Zeeman terms only for centers with spins $S_i = 1/2$:

$$\hat{H}_i = \mu_B \vec{B}_0 \cdot \tilde{g}_i \cdot \hat{\vec{S}}_i \qquad \text{(Eq. 3)}$$

For the reduced medial [3Fe-4S] cluster with spin $S_i = 2$, zero-field splitting was included:

$$\hat{H}_i = \mu_B \vec{B}_0 \cdot \tilde{g} \cdot \hat{\vec{S}}_i + D\,[\hat{S}_{i,z}^2 - 1/3\,S(S+1) + E/D\,(\hat{S}_{i,x}^2 - \hat{S}_{i,y}^2)], \qquad \text{(Eq. 4)}$$

where D and E/D are the axial zero-field splitting and rhombicity parameters. Since EPR measurements of super-oxidized Hase I had revealed isotropic spin coupling between NiB (S_1=1/2) and the proximal cluster (S_2=1/2), as well as with the medial cluster (S_3=1/2), inter-cluster coupling with linear topology was explicitly included in the electronic spin Hamiltonian (see also Fig. S4):

$$\hat{H}_{1,2,3} = -2J_{12}\hat{\vec{S}}_1 \cdot \hat{\vec{S}}_2 - 2J_{23}\hat{\vec{S}}_2 \cdot \hat{\vec{S}}_3 + \sum_{i=1:3} \mu_B \vec{B}_0 \cdot \tilde{g}_i \cdot \hat{\vec{S}}_i, \qquad \text{(Eq. 5)}$$

for which the exchange coupling constants J_{ij} and the relative orientations of the g matrices were taken from the EPR measurements (Table S5).

The magnetic hyperfine interaction, $\hat{\vec{I}} \cdot \tilde{A} \cdot \hat{\vec{S}}_i$, for each electronic spin center i was treated as part of the nuclear Hamiltonians, $\hat{H}_{nuc,j}$, for every iron site j, according to the usual assumption that nuclear and electronic spin systems are decoupled and can be separated due to dominating Zeeman interaction. In this approximation the electronic spin operators for the total spins of the paramagnetic centers (i.e. the FeS clusters and Ni-B) can be replaced by the spin expectation values $\langle S_i \rangle$:

$$\hat{H}_{nuc,j} = \hat{\vec{I}}_j \cdot \tilde{A}_j \cdot \langle \vec{S}_i \rangle - g_N \mu_N \hat{\vec{I}}_j \cdot \vec{B}_0 + \hat{H}_{Q,j} \qquad \text{(Eq. 6)}$$

where B_0 is the applied field, A_j are the magnetic hyperfine coupling tensors, I_j are the nuclear spins, and $H_{Q,j}$ describes the nuclear quadrupole interaction. In addition, isomer shifts δ were added to the nuclear transition energies. The indices j are labeling the 12 individual iron sites in the system ([NiFe] site, distal and proximal 4Fe clusters, medial 3Fe cluster). Isomer shifts and the combined magnetic and electric quadrupole interaction (eq. 6) have been determined for each of the sites. According to the definitions, the A tensor values are given with respect to cluster spins, such that due to the spin coupling schemes for the different clusters in different oxidation states, the individuals sites can have positive or negative A values, depending on the local spin projection factors for the iron sites. Since intrinsic A values are negative for iron (the isotropic part) due to dominating Fermi-contact contribution, negative A values according to this definition indicate the presence of majority (α) spin population, whereas positive values indicate minority (β) spin population.

Fig. S1 Sequence alignment of the small subunits of biochemically and biophysically well-characterized [NiFe] hydrogenases from: *Aquifex aeolicus* VF5 (NP_213454.1), *Hydrogenovibrio marinus (*Sequence provided by Yoshiki Higuchi*)*, *Paracoccus denitrificans* PD1222 (YP_916874.1), *Xanthobacter autotrophicus* Py2 (YP_001417074.1), *Ralstonia eutropha* H16 (NP_942643.1), *Cupriavidus metallidurans* CH34 (YP_583452.1), *Allochromatium vinosum* DSM 180 (YP_003444258.1), *Thiocapsa roseopersicina* (AAA27409.1), *Escherichia coli* str. K-12 substr. MG1655 (NP_415491.1), *Azotobacter vinelandii* DJ (YP_002802122.1), *Allochromatium vinosum* DSM 180 (YP_003443993.1), *Thiocapsa roseopersicina* (AAC38281.1), *Escherichia coli* str. K-12 substr. MG1655 (NP_417471.1), *Wolinella succinogenes* DSM 1740 (NP_907814.1), *Desulfovibrio vulgaris* str. Miyazaki F (YP_002434696.1), *Desulfovibrio fructosovorans* JJ (AAA23371.2), *Desulfovibrio vulgaris* str. Hildenborough (AAS96397.1), *Desulfomicrobium baculatum* DSM 4028 (YP_003157302).

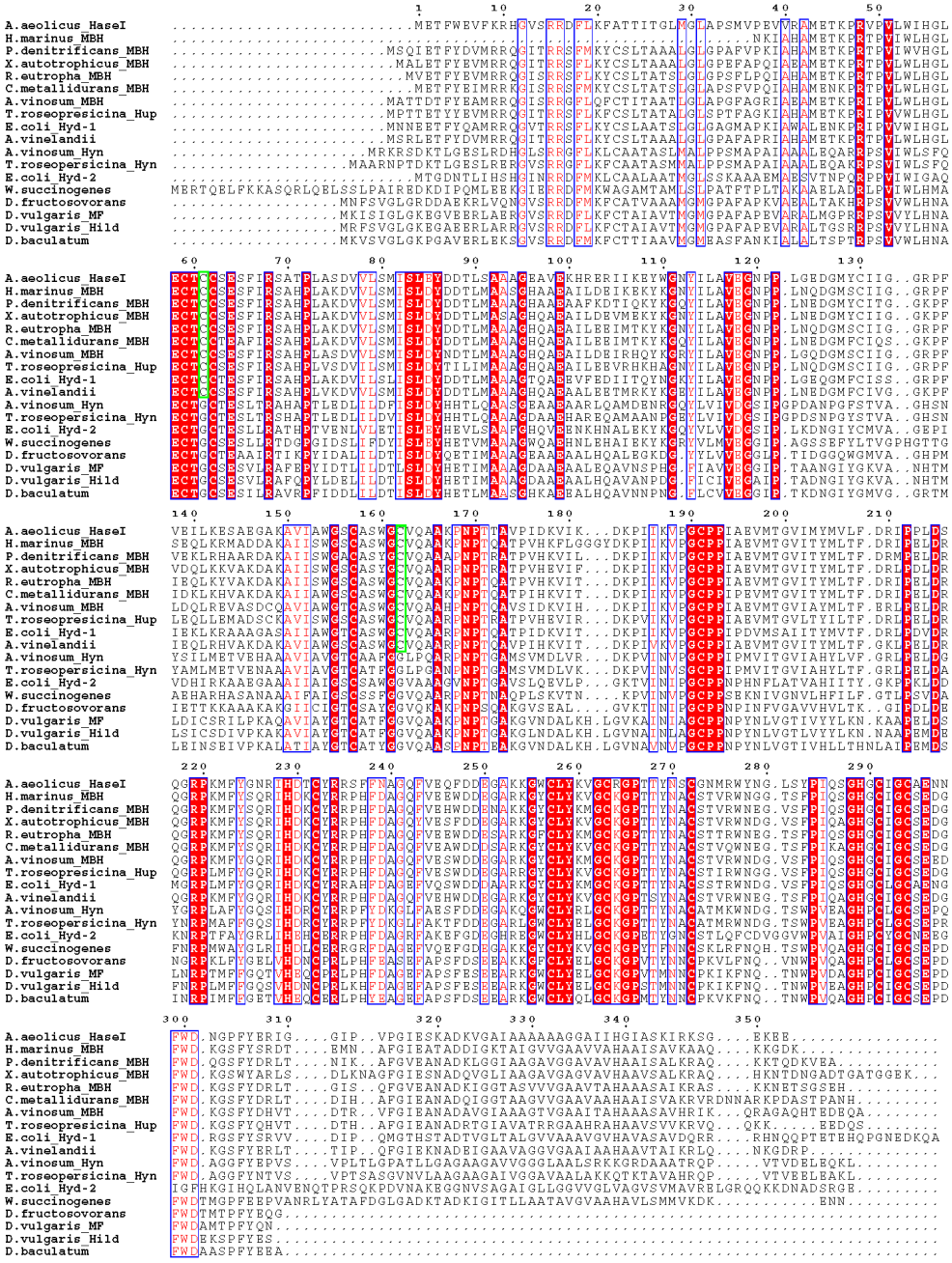

Fig. S2 Pseudo-modulated EPR spectrum of the ^{57}Fe Hase I from *Aquifex aeolicus* after treatment with sodium ascorbate at Q-band. An aliquot of the Mössbauer sample was transferred to the EPR tube and was frozen simultaneously with the sample in the Mössbauer cap after treatment with a 10-fold excess of ascorbate. The dominantly strong radical-like signal in the spectrum at ca. 1210 mT originates from the unreacted porphyrexide radical present in the sample, prior to the partial reduction with ascorbate (see Materials and Methods). The proximal [4Fe-3S] cluster is in its diamagnetic state 4+ (~90%) and the [3Fe-4S] cluster amounts to be more than 90% in its oxidized paramagnetic *S*=1/2 state 1+, as determined from the previous EPR potentiometric titrations and from the amount of the magnetically coupled portion of the sample in our spectrum. There are residual traces of the super-oxidized cluster signal, which would maximally account for ~ 10%. These contributions have been accounted for, for the simulation of the applied field Mössbauer spectra. Experimental conditions: $\pi/2$ = 16 ns, mw Freq. 34.045 GHz, temperature 10K, pseudomodulation was carried out with 4 mT.

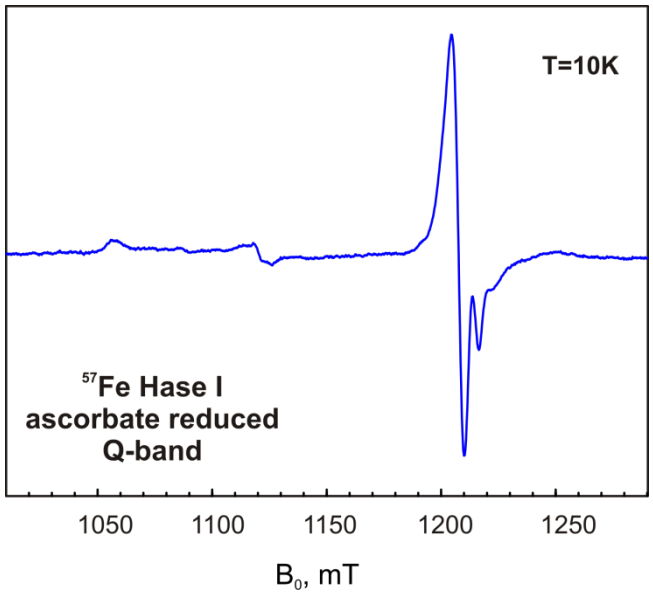

Fig. S3 Uv-visible optical spectra of the as-isolated [NiFe] hydrogenases from *D. vulgaris* MF (16 µM) and *A. aeolicus* (13 µM) recorded at room temperature in 50 mM Tris/HCl pH 7.6. In the aerobically purified enzyme the amount of the proximal centers in the super-oxidized [4Fe-3S]$^{5+}$ state amounts typically to 70-80% . The apparent difference in the extinction coefficient at 408 nm for these two enzymes, harboring the same number of iron-sulfur clusters is likely due to different optical properties of the presence of the [4Fe-3S] cluster in Hase I.

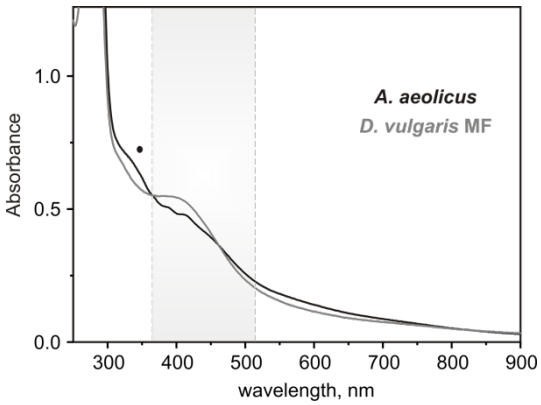

Fig. S4: (A) Linear spin-coupling scheme involving the paramagnetic [NiFe] site in its Ni-B state ($S = 1/2$), the proximal $[4Fe3S]^{5+}$ cluster in its super-oxidized state ($S = 1/2$) and the medial $[3Fe4S]^{1+}$ in its oxidized state ($S = 1/2$), obtained from the simulations of the EPR spectra of the super-oxidized Hase I from *A. aeolicus* (see Table S1). (B) Previously postulated scheme based on the magnetically coupled EPR-spectra of *R. eutropha*. Scheme A is in agreement with the spatial location of the metal cofactors found in the recent crystallographic studies, whereas Scheme B is not.

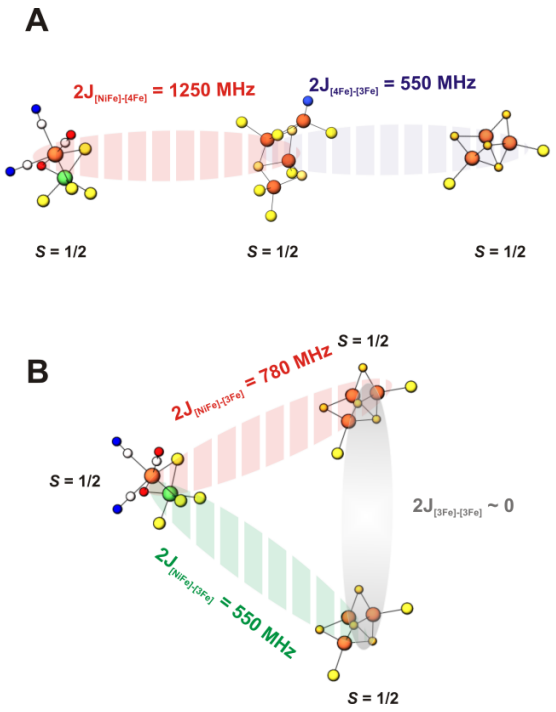

Fig. S5. (A) cw X-band EPR spectrum at 15 K and (B) pseudo-modulated two-pulse echo detected W-band spectrum at 10 K of super-oxidized Hase I with porphyrexide. The spectra have been simulated with a linear three spin exchange model (see text and SI). Experimental conditions: (X-band) mw frequency 9.436 GHz, mw power 2.0 mW, modulation amplitude 1.0 mT; (W-band) mw frequency = 94.03 GHz, $\pi/2$ = 20ns, SRT = 0.5 ms.

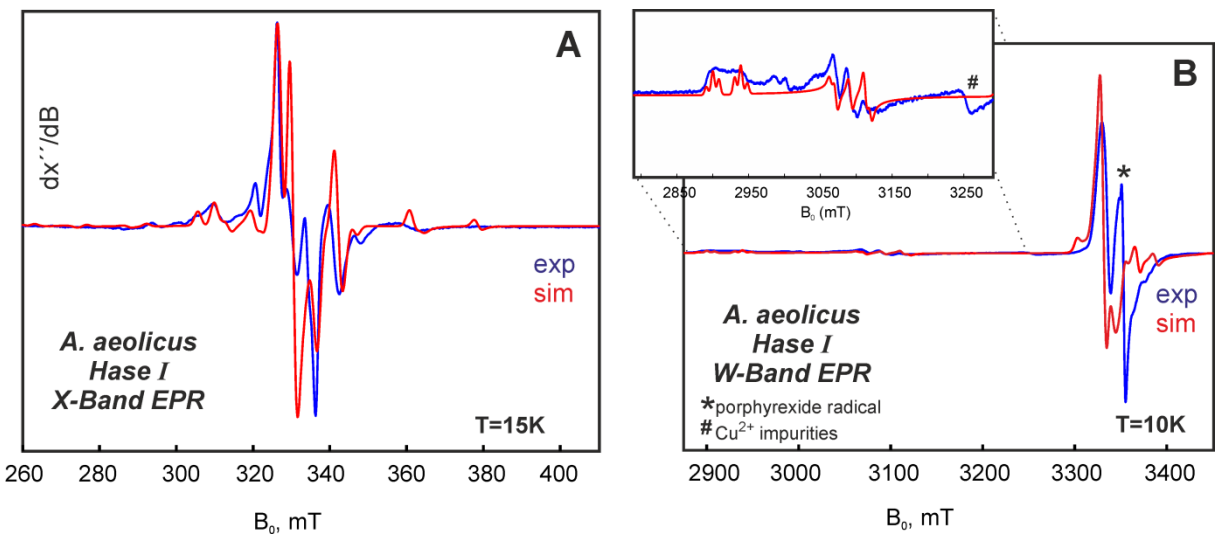

Fig.S6 Mössbauer spectra of the ascorbate reduced Hase I at different applied magnetic fields at 4.2 K. The 7.0 T spectrum at 80 K (fast-relaxation limit) is also included. Experimental traces are shown in black circles and the simulations considering all subcomponents as solid red lines. The individual simulated subspectra are colored as follows: proximal $[4Fe\text{-}3S]^{4+}$ (purple), proximal $[4Fe\text{-}3S]^{5+}$ (magenta), medial $[3Fe\text{-}4S]^{1+}$ (light green), distal $[4Fe4S]^{2+}$ (blue) and the Fe^{2+} of the [NiFe] site (orange),. The simulation parameters for the $[3Fe\text{-}4S]^{1+}$ (medial, light-green color), for the $[4Fe4S]^{2+}$ (distal, blue color), the Fe^{2+} of the [NiFe] site (orange color) are the same as those described for these centers in Table 2 (main manuscript) and Table S2. The diamagnetic $[4Fe\text{-}3S]^{4+}$ has been simulated with parameters (δ = 0.44, 0.44, 0.42 and 0.48 mms^{-1}) and ΔE_Q = (+1.25, +1.1, +1.0 and ± 2.24 mms^{-1}), respectively. From the EPR spectra we have quantified that the amount of the proximal $[4Fe\text{-}3S]^{5+}$ in its super-oxidized state after reduction with ascorbate, is of the order of less than the 10%. This contribution, though minor, has been accounted for in the applied filed simulations using the parameters listed in Table S6. The site-differentiated Fe site with δ = 0.48 mms^{-1} and $|\Delta E_Q|$ = 2.24 mms^{-1} and belongs to the $[4Fe\text{-}3S]^{4+}$ state, shown in purple color. Due to the extended sample degradation after reduction with ascorbate, the amount of adventitiously bound ferric Fe (S=5/2, g = 4.3) was increased and accounted for 9% of the total sample absorption (shown in light-blue color). The contribution of this Fe impurities were simulated considering that even at 80K we are at the slow relaxation-limit with parameters: δ = 0.40 mms^{-1}/ ΔE_Q = 0.32 mms^{-1} and $A_{xyz}/g_N\mu_N$ = (35.6, 57.1, 34.1) T. Due to superposition of these impurities signals in the high-temperature spectra, the sign of the quadrupole coupling of the 'special' site cannot be at present unambiguously identified. A positive value ΔE_Q may be more likely, though still uncertain.

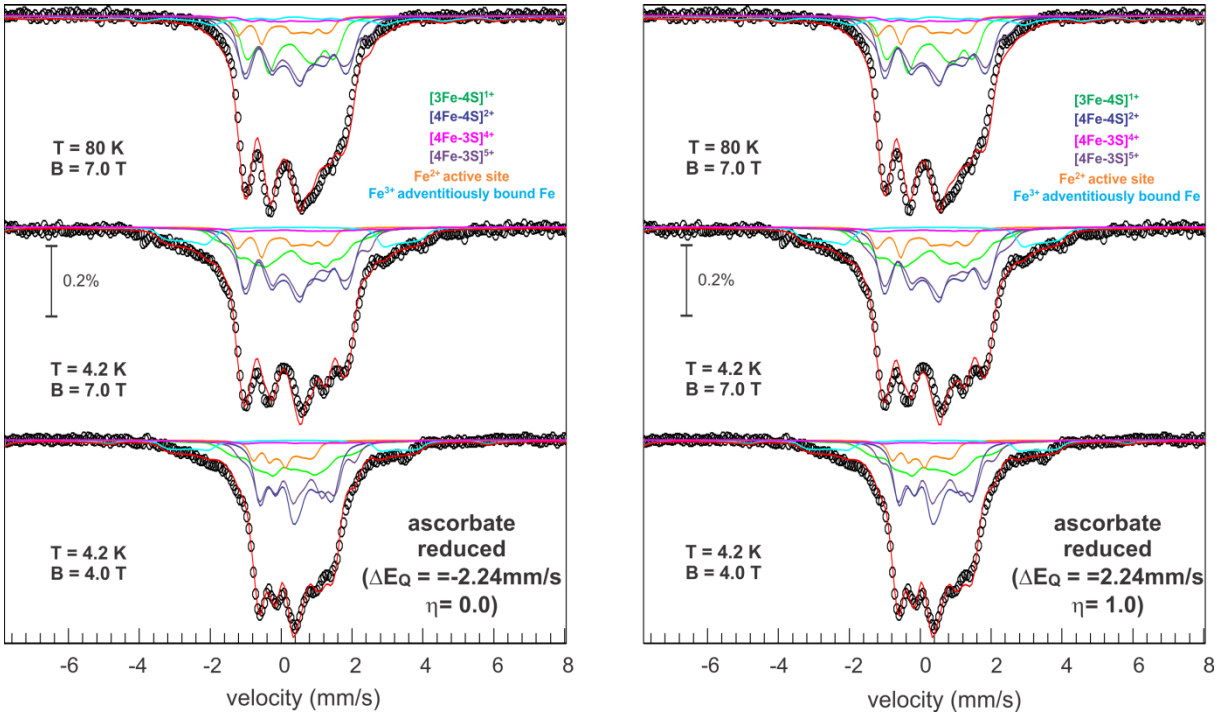

Figure S7. Visualization of the effect of weak spin coupling for the Mössbauer spectra of a single iron site in a paramagnetic center which is part of a spin triad as shown in Figure S4. The green lines shows simulations for a magnetically isolated site without spin coupling with $S_1 = 1/2$ and g values $g_1 = (2.005, 2.014, 1.98)$ as found for the proximal cluster in super-oxidized Hase I. Mössbauer parameters $\delta = 0.4$ mm/s, line width 0.26 mm/s, $\Delta E_Q = +1$ mm/s, $\eta = 0$, and isotropic A tensor, $A/g_N\mu_N = -30$ T, calculated for applied fields of 0.1, 1, 3 and 7 Tesla applied perpendicular to the γ-rays at 4.2 K, assuming slow spin relaxation. The red lines are obtained with the same Mössbauer parameters but with isotropic coupling of the Mössbauer atom to two other spins $S_{2,3} = 1/2$ with $g_2 = (2.3, 2.17, 2.01)$, $g_3 = (2.015, 2.02, 2.015)$, and $J_{12} = 0.021$ cm^{-1}, $J_{13} = 0.0091$ cm^{-1}. The observed 'uncoupling' with increasing strength of the applied field reflects increasing mixing of total spin states, $S_t = 1/2$, 1/2, 3/2 by the Zeeman interaction. This behavior depends critically on the difference of g values for the different sites, and since local g values are anisotropic uncoupling is also orientation dependent and different for different molecules in powder samples. We note that the observed effect for real four- or three iron clusters is less significant than in the model case shown here because anisotropic hyperfine interaction yields 'smearing' of the magnetic splitting for the individuals sites already without inter-cluster coupling. Moreover, intra-cluster coupling yields superpositions of subspectra with positive and negative A-values, which show competing trends.

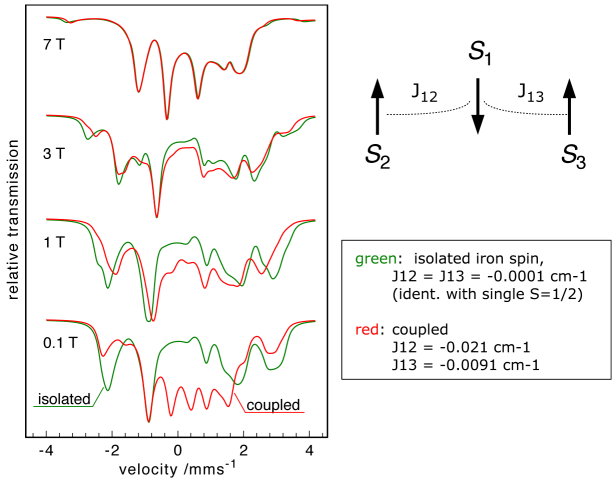

Table S1. Distribution of formal oxidation states in the FeS centers of *A. aeolicus* Hase I. Arrows indicate the spin orientations of the iron sites arising from exchange and double exchange interaction.

	S	"Fe^{2+}"	"$Fe^{2.5+}$"	"Fe^{3+}"
$[4Fe4S]^{1+}$	1/2	2 (↓↓)	2 (↑↑)	-
$[4Fe4S]^{2+}$	0	-	2+2 (↑↑↓↓)	-
$[3Fe4S]^{0}$	2	-	2 (↑↑)	1 (↓)
$[3Fe4S]^{1+}$	1/2	-	-	3 (↑↓↑)
$[4Fe3S]^{3+}$	1/2	2 (↓↓)	2 (↑↑)	-
$[4Fe3S]^{4+}$	0	-	2+2 (↑↑↓↓)	-
$[4Fe3S]^{5+}$	1/2	-	2 (↑↑)	2 (↓↓)[a)]

a) Sub-spin of the 'ferric' pair: $S^* = 4$ like in oxidized HiPIP-type clusters (7)

Table S2. Mössbauer parameters of H_2-reduced Hase I from *A. aeolicus* measured at T = 160K without an applied magnetic field. (Fig. 2 in the main text). Six subspectra have been used that are labeled as shown in the first line. These are 'average' isomer shifts and ΔE_Q splitting, due to the severe overlap of all these Fe sites. The 'true' ones are not distinguishable; therefore the discrimination of Fe^{2+} and $Fe^{2.5+}$ centers is not possible. The relative intensities of each simulated sub-spectrum are also given. Deviations in the percentages from their ideal values (i.e. 8.3% for a genuine Fe site) are attributed to the contribution of Fe impurities in the spectra.

	"Fe^{2+}" or "$Fe^{2.5+}$"	"Fe^{3+}"	"S"	"F"	[NiFe] (Ni-R)
δ, mms^{-1}	0.41/0.42	0.27	0.51	0.72	0.13
ΔE_Q, mms^{-1}	1.29/0.80	0.60	2.61	1.56	0.44
rel. Int.	41.0 /27.0	8.3%	8.6%	7.6%	7.5 %
sites	8	1	1	1	1

Table S3. Mössbauer parameters of oxidized Hase I from *A. aeolicus* (treated with ascorbate) measured at T = 160K without an applied magnetic field. (Fig. 3 in the main text). Five subspectra have been used that are labeled as shown in the first line. These are 'average' isomer shifts and ΔE_Q splitting, due to the severe overlap of all these Fe sites. The relative intensities of each simulated sub-spectrum are also given. Deviations in the percentages from their ideal values (i.e. 8.3% for a genuine Fe site) are attributed to the contribution of Fe impurities in the spectra.

	"$Fe^{2.5+}$"	"Fe^{3+}"	"S"	[NiFe] (Ni-B)
δ, mms^{-1}	0.41/0.41	0.24	0.48	0.05
ΔE_Q, mms^{-1}	1.20/0.80	0.63	2.23	0.59
rel. Int.	26.5%/30.7%	25.7%	8.3%	8.3%
sites	7	3	1	1

Table S4. Mössbauer parameters of super-oxidized Hase I from *A. aeolicus* (treated with porphyrexide) measured at T = 160K without applied magnetic field. (Fig. 3 in the main text). Five subspectra have been used that are labeled as shown in the first line. These are 'average' isomer shifts and ΔE_Q splitting, due to the severe overlap of all these Fe sites. The relative intensities of each simulated sub-spectrum are also given. Deviations in the percentages from their ideal values (i.e. 8.3% for a genuine Fe site) are attributed to the contribution of Fe impurities in the spectra.

	"$Fe^{2.5+}$"	"Fe^{3+}"	"S"	[NiFe] (Ni-B)
δ, mms^{-1}	0.39/0.51	0.27	0.46	0.08
ΔE_Q, mms^{-1}	0.89/1.04	0.59	2.42	0.56
rel. Int.	28.5% /15%	42%	7.0%	8.3%
sites	5	5	1	1

Table S5: Electronic parameters obtained from the simulations of the EPR spectra of the super-oxidized Hase I from *A. aeolicus* carried out in four different microwave frequencies (S-, X-, Q- and W-Band). Based on these simulations, the linear coupling scheme between the [NiFe] site (S=1/2), the proximal $[4Fe3S]^{5+}$ cluster (S=1/2) and the medial $[3Fe4S]^{1+}$ cluster has been constructed (S=1/2), as shown in Fig. S3. α, β, γ are the tilt angles (Euler) of the g-tensor with respect to the molecular frame. Additionally for spectra recorded at the different microwave frequencies an orientation-dependent phenomenological broadening has been included to include effects from unresolved hyperfine couplings. The x,y,z notations in the description of the principal values of the given iron-sulfur cofactors are according to the general nomenclature of these centers and do not correspond to their orientation with respect to the molecular frame.

	Ni-B	**$[4Fe3S]^{5+}$**	**$[3Fe4S]^{1+}$**
g_x	2.300	2.015	2.022
g_y	2.171	2.004	2.018
g_z	2.010	1.980	2.010
α	0	30	20
β	0	0	50
γ	0	40	110

$2J_{NiB\text{-}[4Fe3S]}$	**$2J_{NiB\text{-}[3Fe4S]}$**	**$2J_{[4Fe3S]\text{-}[3Fe4S]}$**
1250 MHz ($0.04169\ cm^{-1}$)	0	550 MHz (0.0183 cm-1)

Table S6. Mössbauer parameters and hyperfine tensors of the metal cofactors in the H_2 reduced state of the *A. aeolicus* Hase I. For the 6C proximal cluster, these parameters can be interpreted using the classical coupling scheme of conventional cubane clusters in the 1+ state. The spectra are best simulated assuming that the special site S belongs to the ferrous pair (positive *A*) and the second special site F is part of the delocalized pair (negative *A*). The data can be also fitted assuming that the two special sites belong to the ferrous pair (positive *A*). However, the latter cannot be reproduced by the density functional studies performed in this study, which clearly support the assignment of the second special site F to the valence delocalized pair ($Fe^{2.5+}$-$Fe^{2.5+}$).

	$[4Fe\text{-}3S]^{3+}$ (proximal)	$[3Fe\text{-}4S]^{0}$ (medial)	$[4Fe\text{-}4S]^{1+}$ (distal)	[NiFe] (Ni-R state)
δ , mms^{-1}	+0.71	+0.30	+0.45	+0.13
	+0.44	+0.43	+0.44	
	+0.42	+0.45	+0.42	
	+0.50	-	+0.43	
ΔE_Q , mms^{-1}	+1.52	+0.60	+1.06	+0.56
	+1.23	+1.44	+1.03	
	+0.84	+1.32	+0.92	
	+2.60	-	+0.96	
η	0.30	1.00	0.80	
	0.90	0.50	0.00	
	0.30	0.50	0.50	
	0.10	-	0.00	
$A_{xx}/g_N\mu_N$, T	-30.0	+6.0	+2.2	
	+12.0	-16.0	+2.2	
	-15.0	-16.0	-28.0	
	+12.0	-	-28.0	
$A_{yy}/g_N\mu_N$, T	-32.0	+12.0	+2.2	
	+22.0	-15.0	+2.2	
	-30.0	-15.0	-24.0	
	+15.0	-	-24.0	
$A_{zz}/g_N\mu_N$, T	-32.0	+12.7	+2.2	
	+26.0	-12.3	+2.2	
	-30.0	-12.3	-4.0	
	+15.0	-	-4.0	
α ,°	0	0	0	
	0	40	90	
	0	40	90	
	0	-	0	
β ,°	40	20	0	
	0	20	40	
	0	0	40	
	0	-	0	
γ , °	0	0	0	
	0	0	0	
	0	0	0	
	0	0	0	
	0	-	0	
D , cm^{-1}		-2.20		
E/D		0.26		

Table S7. Mössbauer parameters and hyperfine tensors of the metal cofactors in the super-oxidized state of the *A. aeolicus* Hase I. The [4Fe-3S] proximal cluster in its 5+ state is isoelectronic with the 3+ classical cubanes occuring in HiPIP proteins and indeed the experimental data can be well accounted for considering the coupling scheme of high-potential cubane centers. However, due to the distorted nature of the cluster, a coupling scheme that is different from that of HiPIP-like clusters would be more suitable. This modified scheme, also previously suggested by a recent theoretical and crystallographic study, considers formally the coupling scheme of a reduced $[3Fe\text{-}4S]^0$ cluster (an Fe^{3+} antiferromagnetically coupled to a mixed-valence delocalized pair $Fe^{2.5+}$-$Fe^{2.5+}$) antiferromagnetically coupled to the fourth Fe^{3+} site of the [4Fe-3S] moiety. In this model the mixed valence pair would have positive *A* and the ferric pair would have negative *A*. The signs of the hyperfine tensors would be similar to those encountered in conventional HiPIP centers, however the magnitudes are different due to the different spin-projection factors (Clebsch-Gordan coefficients) (8) .

	$[4Fe\text{-}3S]^{5+}$ (proximal)	$[3Fe\text{-}4S]^{1+}$ (medial)	$[4Fe\text{-}4S]^{2+}$ (distal)	[Ni**Fe**] (Ni-B state)
δ , mms^{-1}	+0.40	+0.29	+0.45	+0.10
	+0.46	+0.28	+0.44	
	+0.39	+0.28	+0.41	
	+0.28	-	+0.45	
ΔE_Q , mms^{-1}	-1.00	+0.62	+1.27	+0.60
	+2.45	+0.62	+1.08	
	+0.70	+0.62	+0.97	
	+0.60	-	+1.27	
η	0.70	0.90	1.00	
	0.50	0.20	0.00	
	1.00	0.20	1.00	
	0.30	-	1.00	
$A_{xx}/g_N\mu_N$, T	-17.0	-18.0		
	+5.1	+9.0		
	-9.3	+2.5		
	+20.0	-		
$A_{yy}/g_N\mu_N$, T	-13.0	-27.8		
	+30.3	+9.0		
	-51.0	+2.5		
	+25.3	-		
$A_{zz}/g_N\mu_N$, T	-43.0	-29.0		
	+20.3	+9.0		
	-43.9	+2.5		
	+27.4	-		
α , °	0	0		
	0	0		
	0	0		
	0	-		
β , °	0	0		
	0	0		
	0	25		
	0	-		
γ , °	0	0		
	0	0		
	0	0		
	0	-		

The sign of the quadrupole splittings for the super-oxidized cluster cannot be assigned with full confidence due to the complexity of the spectra and the contributions of Fe degradation impurities. Therefore, the more plausible solution for the sign of the quadrupole splitting has been taken as the one that best describes both the experimental and the theoretical calculations performed in the present study.

Note that the experimental data were extracted from the samples oxidized in air. By this procedure 80% of the proximal [4Fe-3S] cluster is in its super-oxidized state (5+) and the rest in the diamagnetic 4+ state. Whereas treatment with porphyrexide yields 100% of the proximal [4Fe-3S] cluster in its 5+ state, such a preparation has the drawback that it leads to extensive sample degradation. Therefore, first the data of the air-oxidized enzyme were fitted accounting for 80% of the proximal cluster in its 5+ state, and then the data of the porphyrexide oxidized Hase I were fitted assuming 100% super-oxidation of the proximal cluster.

Computational Section

Computational Details

The calculations for the proximal [4Fe-3S] cluster of hydrogenase I from *Aquifex Aeolicus* were carried out using the ORCA quantum chemistry program package.[9] Initial geometries were cut out from the crystal structures of both super-oxidized and reduced forms of the membrane-bound [NiFe]-hydrogenase from *H. marinus* (PDB ID 3AYX and 3AYY respectively). All amino acids directly interacting with the iron sulfur cluster core [4Fe-3S], plus Glu_8[10] were retained in the computational models (Fig. S8). The total charge of the super-oxidized species was kept neutral, whereas reduced species obtained a charge of -2, as consistent with two-electron reduction of the iron-sulfur core: $[4Fe\text{-}3S]^{5+} + 2e^- = [4Fe\text{-}3S]^{3+}$. All side chain residues were truncated at the α-carbons. The Glu_{82} group with possibly important interaction with the iron cluster was considered in both its protonated and deprotonated forms (Ox1/Red1 and Ox2/Red2, respectively). Calculations have also been carried out for the intermediate $[4Fe\text{-}3S]^{4+}$ oxidation state (*i.e.* ascorbate reduced). Since the X-Ray crystallographic structure has not been solved, calculations were started both from the structures of the oxidized (labeled as Semiox) and from the reduced (denoted as Semired) states, considering the protonation states as before (Semiox1/2, Semired1/2 for protonated/unprotonated cases).

The starting geometries were then fully optimized within the broken symmetry DFT framework[10,11] with spin populations flipped on pairs of iron centers, setting the total spin equal to $S = 1/2$ ($S = 0$ for Semiox/Semired) as was established in the EPR spectroscopic investigations. The centers on which spins are flipped are indicated after an underscore, e.g. Ox1_12 corresponds to centers Fe1 and Fe2 flipped (super-oxidized species with Glu_{82} protonated). Note that there are only half as many spin flip cases for Semiox and Semired structures. The positions of α-carbons of amino acids (altogether seven) were kept frozen during the optimization. In total 24 models were optimized for the super-oxidized (Ox) and the fully reduced (Red) species, and 24 for the intermediate oxidation state using the PBE functional[12,13]and double-ζ quality SV(P) basis set,[14] applied for all atoms. The conductor-like screening model (COSMO)[15] was applied to account for solvent effects with a dielectric constant of 4, and the zero-order regular approximation (ZORA)[16,17] to account for relativity. The keyword

TightSCF was used in all cases requesting that total energies converge to 10^{-7} hartree. Geometry optimizations were performed with a convergence threshold of 10^{-4} for the RMS gradient and 3×10^{-4} for the maximum component of the gradient (in hartree/bohr units).

Various Mössbauer parameters were then obtained from PBE/TZVP[18] and B3LYP[19,20]/TZVP single point calculations on the optimized structures. For the calculation of isomer shifts, the test set from Neese *et al.*[21]was used to calibrate our choice of DFT functional and basis set. The calibration procedure consists of calculating the electron density at the nuclei of interest and comparing to the experimentally known isomer shift values. The linear correspondence is then fitted to a straight line using the least squares method (see Fig. S11 a, b). To obtain reliable Mössbauer parameters form DFT calculations an additional flexibility of the basis set in the nuclear region and higher integration accuracy is required. For this purpose the ORCA "core properties" CP(PPP)[9] basis set was used with the radial integration accuracy parameter increased to 9.0 for iron centers.

Nuclear quadruple coupling constants, e^2qQ/h, were calculated from the electric field gradients V_{ii} according to the equation $e^2qQ/h = const*V_{ii}*Q$, where Q is the nuclear quadrupole moment (Q(Fe) = 0.16 barn). The factor const = 234.96 serves to convert e^2qQ/h from atomic to MHz units (whereas 11.6248 MHz correspond to a Doppler velocity of 1mm/s for the 14.412 keV γ-radiation of ^{57}Fe). The deviation of the nuclear quadrupole tensor from axial symmetry is given by the asymmetry parameter $\eta = (V_{xx} - V_{yy})/V_{zz}$ in a coordinate system where $|V_{zz}|>|V_{yy}|>|V_{xx}|$.

Fermi contact terms and spin-dipole contributions to the hyperfine coupling (HFC) tensor were calculated as expectation values using PBE and B3LYP. Second order contributions to the hyperfine couplings that arise from spin-orbit coupling (SOC) were obtained using coupled perturbed Kohn-Sham theory.[22] The spin orbit coupling (SOC) operator was treated by the spin-orbit mean-field (SOMF) approximation to the Breit-Pauli operator.[23]

For the purpose of analysis, the unrestricted Kohn-Sham orbitals were transformed into the quasi-restricted orbitals (QROs)[24] which were then localized according to Pipek-Mezey localization procedure.[25] Orbitals, densities and structures were visualized with the Chimera program.[26]

Geometries and Electronic Structure

Comparing the optimized structures to those obtained from X-Ray crystallographic investigations (see Table S8), we may conclude in general good agreement. Typically, the deviation in bond lengths were smaller than ~0.1 Å. Furthermore, structures with the Glu_{82} deprotonated tend to agree better with the experimental values. In the super-oxidized species, the characteristic Fe2-N bond is reproduced in all optimized structures. It is also important to point out that in the super-oxidized structures (denoted as Ox), the characteristically large distance between Fe2 and S3, albeit somewhat varied during the optimization, remained significantly large. Similar agreement between experiment and theory may be observed in the reduced models, where the initial structures were already closer to the cubane arrangement. The structure Red2_24 seems to be an exception, as in this case the optimization yielded a more tightly closed cubane structure as indicated by the significantly smaller Fe2-Fe4 distance (Red2_24: 2.81 Å vs. Exp.: 3.98 Å). The elongation of the Fe4-Sγ(Cys126) distance (from 2.35 Å to 4.25 Å) in this case also indicates a corresponding bond break parallel to the closure of the iron-sulfur cluster.

Related to the geometrical arrangement is the short distance between some iron sites, which indicates the presence of some partial bond, and which is also supported by the analysis of orbitals shown in Fig. S9. In the super-oxidized case, this interaction is significant (Mayer bond order[27] 0.6) only between Fe1 and Fe3, whereas in the more compact reduced state the interaction occurs between both iron pairs, which is typical for the cubane electronic structure. The metal-metal interaction is of great importance as it is the basis for exchange coupling interactions and thus assigning delocalized pairs. In fact, for most preferable model Ox2_24 has a delocalized mixed-valence iron pair 1-3. Finally, spin density plots have also been produced, and are shown in Fig. S10. The iron centers Fe1 and Fe3 have the same sign for spin density, which is the opposite to that on Fe2 and Fe4. This observation agrees with indications from spin population and A_{iso} data in the main text.

Calculation of Mössbauer parameters

With regard to spectroscopic parameters, several factors were considered in matching the experimental and theoretical data. Energetic differences between various broken symmetry states were only considered a decisive factor while eliminating a possible electronic arrangement, if the candidate was significantly higher in energy than the lowest lying state (i.e. more than 4-5 kcal/mol). Similarly, the sign of the quadrupole splitting was only considered strictly if they belonged to a sufficiently small asymmetry parameter ($\eta < 0.9$). Oxidation states may be assigned on the basis of isomer shifts. Considering all these factors, it may be stated that the agreement between experiment and theory for the oxidized state is somewhat better than for the reduced state, nevertheless, it was possible to come up with a most likely assignment for both cases. These results have been discussed in the main text in connection with the most likely candidates. In Tables S9 and S10, calculated spectroscopic data for all broken symmetry cases are given for the PBE functional. Corresponding B3LYP results are shown in Tables S12 and S13.

Calculations on the intermediate oxidation state (super-oxidized cluster + e^-) were also conducted. Tables S11 and S14 contain all calculated spectroscopic data for the semioxidized models using the PBE and B3LYP functionals, respectively. Since firm experimental data are available only for the Ox and Red species, these results are to be evaluated with caution. The only strong feature expected experimentally for the intermediate oxidation state is a large quadruple splitting for one of the irons, indicating an unusual coordination. This could not be reproduced in the presented calculations, indicating the possibility of some missing structural feature (e.g. a water molecule not seen in the crystal structures available). Since the purpose of this paper was to shed light on the properties of the two oxidation states discussed in the main text, this aspect was not investigated in any further detail.

Table S8. Geometrical data calculated for all BS-species of super-oxidized (OX) and reduced (Red) states of the [4Fe 3S] model cluster. Distances are given in Å units.

	Fe2-N (Cys26)	Fe2-Sγ (Cys26)	Fe2-Sγ (Cys25)	Fe2-S2	Fe2-S3	Fe2-Fe1	Fe2-Fe3	Fe2-Fe4	Fe4-Sγ (Cys158)	Fe4-Sγ (Cys126)
Exp_Ox	2.09	2.31	2.51	2.31	4.01	3.10	3.82	5.36	2.24	2.31
Ox1_12	1.91	2.18	2.30	2.24	3.92	2.82	3.62	5.08	2.33	2.28
Ox1_13	1.90	2.19	2.24	2.23	3.94	2.61	3.26	4.78	2.30	2.29
Ox1_14	1.95	2.27	2.26	2.30	3.85	2.63	3.49	4.76	2.29	2.29
Ox1_23	1.89	2.21	2.22	2.27	4.06	2.62	3.53	4.83	2.30	2.30
Ox1_24	1.88	2.20	2.23	2.19	4.11	2.68	3.53	4.87	2.30	2.28
Ox1_34	1.97	2.28	2.35	2.34	3.61	2.68	3.33	4.80	2.26	2.24
Ox2_12	1.91	2.23	2.49	2.32	4.73	3.11	4.19	5.50	2.29	2.36
Ox2_13	2.02	2.26	2.74	2.39	4.76	3.36	4.14	5.74	2.28	2.36
Ox2_14	2.01	2.28	2.51	2.55	4.86	3.13	4.30	5.70	2.27	2.35
Ox2_23	1.90	2.23	2.47	2.36	4.79	3.21	4.14	5.60	2.28	2.35
Ox2_24	1.93	2.22	2.43	2.34	4.82	3.21	4.15	5.72	2.30	2.36
Ox2_34	2.01	2.27	2.61	2.55	4.75	3.39	4.25	5.61	2.29	2.36
Exp_Red	3.25	2.31	2.38	2.30	2.39	2.78	2.80	3.98	2.28	2.35
Red1_12	3.58	2.32	2.42	2.28	2.29	2.56	2.68	3.68	2.35	2.40
Red1_13	3.44	2.24	2.34	2.24	2.31	2.64	2.65	3.79	2.32	2.58
Red1_14	3.42	2.28	2.36	2.30	2.31	2.63	2.61	3.70	2.29	2.55
Red1_23	3.38	2.27	2.40	2.24	2.33	2.64	2.60	3.70	2.31	2.43
Red1_24	3.41	2.23	2.29	2.26	2.32	2.62	2.71	3.83	2.36	2.43
Red1_34	3.45	2.31	2.39	2.27	2.23	2.84	2.59	3.71	2.38	2.45
Red2_12	3.68	2.27	2.33	2.25	2.30	2.56	2.72	3.74	2.37	2.55
Red2_13	3.57	2.25	2.30	2.23	2.36	2.81	2.69	3.76	2.32	2.67
Red2_14	3.61	2.31	2.43	2.25	2.37	2.65	2.55	3.80	2.28	2.33
Red2_23	3.48	2.24	2.28	2.22	2.32	2.70	2.62	3.74	2.30	2.72
Red2_24	3.50	2.25	2.30	2.22	2.32	2.88	2.70	2.81	2.27	4.25
Red2_34	3.71	2.27	2.37	2.27	2.25	2.80	2.64	3.66	2.34	2.68

Table S9. Spectroscopic data calculated for all BS-species of the super-oxidized $[4Fe\text{-}3S]^{5+}$ model cluster using the PBE functional. Energy differences (ΔE) are given in kcal/mol with respect to the lowest energy species. Isomer shifts (δ) and quadrupole splittings (ΔE_Q) are given in mms^{-1} units. The asymmetry parameter (η) is unitless, whereas the isotropic hyperfine coupling (A_{iso}) values are presented in MHz units (A = 1 MHz corresponds to an internal field $A/g_N\beta_N = 0.7238$ T).

species	ΔE	δ	η	ΔE_Q	A_{iso}	spin pop.
Ox1_12	21.39	0.32	0.64	1.19	52.4	-3.2
		0.19	0.15	2.33	9.4	-2.5
		0.20	0.46	-1.16	-50.2	3.0
		0.26	0.61	-1.18	-59.1	3.3
Ox1_13	1.73	0.33	0.35	0.78	43.6	-2.4
		0.17	0.24	2.02	-16.7	2.3
		0.21	0.25	0.95	43.2	-2.7
		0.21	0.51	-0.40	-59.9	3.4
Ox1_14	0.00	0.32	0.18	1.67	27.6	-2.5
		0.21	0.79	1.27	-51.1	3.5
		0.16	0.33	0.67	-43.4	3.0
		0.20	0.46	-0.61	50.6	-3.4
Ox1_23	2.73	0.35	0.16	1.32	-35.8	2.7
		0.20	0.18	2.17	9.6	-2.3
		0.17	0.27	0.72	44.5	-3.0
		0.20	0.69	0.63	-50.2	3.4
Ox1_24	2.85	0.41	0.73	-1.74	-56.5	3.1
		0.13	0.13	2.15	13.6	-2.1
		0.25	0.18	0.61	-55.4	3.2
		0.17	0.86	0.44	59.6	-3.3
Ox1_34	14.31	0.33	0.59	1.56	-56.4	3.3
		0.31	0.94	1.78	-60.2	3.6
		0.20	0.64	-0.82	51.8	-3.1
		0.19	0.40	1.29	47.2	-2.8
Ox2_12	9.04	0.35	0.47	1.38	49.2	-3.0
		0.37	0.65	1.41	54.1	-2.7
		0.25	0.90	-0.72	-53.1	3.0
		0.27	0.91	1.41	-57.6	3.4
Ox2_13	0.00	0.36	0.82	-1.79	57.4	-3.4
		0.41	0.69	-1.03	-76.1	3.7
		0.27	0.80	0.81	55.2	-3.2
		0.19	0.95	0.78	-57.9	3.4
Ox2_14	2.18	0.37	0.05	2.21	36.6	-2.9
		0.42	0.33	-0.95	-76.1	3.8
		0.18	0.23	0.44	-47.7	3.0
		0.21	0.77	-0.98	46.8	-3.4

Ox2_23	1.48	0.41	0.17	2.01	-40.1	3.0
		0.39	0.61	1.97	49.1	-2.6
		0.17	0.37	0.60	45.7	-3.0
		0.22	0.75	-0.89	-48.8	3.4
Ox2_24	3.95	0.39	0.83	-1.56	-60.3	3.3
		0.38	0.40	2.25	49.0	-2.4
		0.30	0.74	0.81	-57.9	3.3
		0.22	0.56	0.74	58.9	-3.4
Ox2_34	8.52	0.30	0.74	1.19	-48.5	3.3
		0.43	0.51	-1.12	-74.9	3.8
		0.25	0.61	1.02	54.0	-3.1
		0.26	0.90	-1.58	53.9	-3.3

Table S10. Spectroscopic data calculated for all BS-species of the reduced $[4Fe\text{-}3S]^{3+}$ model cluster using the PBE functional. Energy differences (ΔE) are given in kcal/mol with respect to the lowest energy species. Isomer shifts (δ) and quadrupole splittings (ΔE_Q) are given in mms^{-1} units. The asymmetry parameter (η) is unitless, whereas the isotropic hyperfine coupling (A_{iso}) values are presented in MHz units (A = 1 MHz corresponds to an internal field $A/g_N\beta_N = 0.7238$ T).

Species	ΔE	δ	η	ΔE_Q	A_{iso}	spin pop.
Red1_12	0.53	0.41	0.41	1.39	52.5	-3.0
		0.46	0.97	1.66	55.8	-3.1
		0.30	0.58	0.45	-48.3	3.1
		0.38	0.46	1.53	-64.7	3.6
Red1_13	8.91	0.44	0.43	1.87	42.1	-2.7
		0.35	0.97	1.52	-34.6	3.0
		0.32	0.94	1.25	39.4	-2.8
		0.47	0.84	1.45	-37.7	3.2
Red1_14	7.61	0.38	0.35	2.24	29.9	-2.7
		0.36	0.69	-1.21	-56.9	3.3
		0.33	0.83	-1.03	-49.9	3.1
		0.48	0.27	2.47	33.7	-3.2
Red1_23	0.00	0.41	0.25	1.82	-31.5	3.0
		0.50	0.04	1.35	38.2	-2.7
		0.31	0.81	-0.90	44.0	-2.9
		0.33	0.47	0.93	-50.8	3.4
Red1_24	4.39	0.39	0.80	-1.60	-56.7	3.3
		0.37	0.48	-2.08	33.7	-2.7
		0.32	0.47	0.93	-54.5	3.2
		0.47	0.35	2.14	48.9	-3.1
Red1_34	11.08	0.52	0.29	2.10	-54.5	3.5
		0.44	0.62	-1.86	29.0	-2.8

		0.31	0.69	1.32	-48.0	3.1
		0.51	0.44	2.18	39.1	-3.3
Red2_12	16.80	0.47	0.35	1.45	46.8	-3.0
		0.38	0.68	-1.65	52.4	-3.0
		0.32	0.47	-0.49	-49.8	3.1
		0.46	0.80	2.13	-49.9	3.5
Red2_13	17.72	0.67	0.98	1.02	54.1	-3.1
		0.35	0.95	-0.91	-41.8	3.2
		0.37	0.92	-1.19	35.9	-2.7
		0.48	0.85	1.51	-33.9	3.3
Red2_14	0.00	0.38	0.92	-2.05	30.9	-2.7
		0.43	0.83	-1.74	-40.9	3.2
		0.28	0.51	-0.50	-50.6	3.1
		0.41	0.16	3.05	31.3	-3.0
Red2_23	15.01	0.55	0.96	1.15	-41.4	3.3
		0.39	0.76	1.22	37.7	-2.6
		0.34	0.47	1.20	45.5	-3.0
		0.48	0.38	1.99	-29.0	3.2
Red2_24	2.97	0.60	0.28	1.41	-63.4	3.5
		0.35	0.99	1.25	43.8	-3.1
		0.36	0.30	0.93	-50.1	3.1
		0.46	0.51	2.13	26.6	-2.7
Red2_34	13.41	0.56	0.93	1.78	-49.1	3.3
		0.35	0.88	1.10	-57.9	3.3
		0.33	0.46	0.71	41.3	-2.8
		0.57	0.51	1.52	49.0	-3.2

Table S11. Spectroscopic data calculated for all BS-species of the semioxidized/semireduced [4Fe-3S]$^{4+}$ model cluster using the PBE functional. Energy differences (ΔE) are given in kcal/mol with respect to the lowest energy species. Isomer shifts (δ) and quadrupole splittings (ΔE_Q) are given in mms^{-1} units. The asymmetry parameter (η) is unitless.

species	ΔE	δ	η	ΔE_Q	spin pop.
Semiox1_12	10.87	0.40	0.75	-0.91	3.2
		0.34	0.59	1.06	3.5
		0.32	0.38	-1.07	-3.2
		0.29	0.73	1.00	-3.4
Semiox1_13	0.00	0.43	0.60	-0.95	-3.0
		0.25	0.73	1.18	2.4
		0.36	0.56	-1.05	-3.2

		0.21	0.41	0.96	3.4
Semiox1_14	1.08	0.41	0.77	-0.95	2.7
		0.32	0.58	1.12	-3.4
		0.27	0.27	-1.08	-2.8
		0.23	0.60	1.02	3.4
Semiox2_12	1.59	0.39	0.75	1.09	3.1
		0.47	0.64	0.73	3.8
		0.33	0.32	-0.98	-3.3
		0.33	0.86	1.02	-3.5
Semiox2_13	1.83	0.48	0.93	1.08	-2.9
		0.44	0.66	0.82	2.6
		0.36	0.44	-0.94	-3.2
		0.27	0.67	1.01	3.4
Semiox2_14	0.00	0.44	0.83	1.12	2.9
		0.49	0.69	0.80	-2.8
		0.26	0.45	-0.98	-3.2
		0.34	0.87	1.05	3.2
Semired1_12	0.00	0.50	0.35	1.23	-3.3
		0.29	0.65	0.93	-3.3
		0.26	0.91	0.89	3.1
		0.43	0.15	1.17	3.5
Semired1_13	1.69	0.54	0.38	1.25	-3.4
		0.30	0.49	0.98	2.8
		0.24	0.65	0.90	-2.8
		0.40	0.12	1.14	3.4
Semired1_14	0.21	0.54	0.13	1.23	-3.2
		0.39	0.67	0.98	3.3
		0.25	0.82	0.87	3.1
		0.37	0.75	1.30	-3.3
Semired2_12	2.67	0.33	0.79	1.17	-3.2
		0.30	0.69	1.04	-3.2
		0.27	0.96	-0.94	3.0
		0.38	0.20	1.17	3.5
Semired2_13	1.56	0.36	0.74	1.18	-3.1
		0.35	0.61	1.12	2.6
		0.24	0.88	0.90	-3.0
		0.30	0.27	1.11	3.4
Semired2_14	0.00	0.36	0.67	1.20	-2.7
		0.31	0.67	1.12	3.2
		0.24	0.97	0.88	2.8
		0.31	0.15	1.12	-3.4

Table S12. Spectroscopic data calculated for all BS-species of the super-oxidized $[4Fe\text{-}3S]^{5+}$ model cluster using the B3LYP functional. Energy differences (ΔE) are given in kcal/mol with respect to the lowest energy species. Isomer shifts (δ) and quadrupole splittings (ΔE_Q) are given in mms^{-1} units. The asymmetry parameter (η) is unitless, whereas the isotropic hyperfine coupling (A_{iso}) values are presented in MHz units.

species	ΔE	δ	η	ΔE_Q	A_{iso}	spin pop.
Ox1_12	15.16	0.17	0.54	1.20	76.57	-3.8
		0.15	0.29	3.96	8.03	-2.8
		0.20	0.69	-1.60	-67.90	3.5
		0.25	0.75	-1.56	-78.78	3.7
Ox1_13	17.84	0.28	0.68	-3.01	65.23	-3.4
		0.03	0.12	1.94	-58.91	3.7
		0.14	0.39	0.91	76.67	-3.6
		0.11	0.71	-0.52	-83.25	3.8
Ox1_14	0.00	0.33	0.20	2.78	42.84	-3.2
		0.11	0.58	1.35	-71.09	3.9
		0.10	0.46	0.77	-65.65	3.6
		0.11	0.30	-0.72	70.77	-3.8
Ox1_23	7.38	0.36	0.23	2.44	-51.10	3.3
		0.15	0.21	2.74	17.18	-2.7
		0.11	0.38	0.82	67.69	-3.6
		0.10	0.49	0.68	-71.16	3.8
Ox1_24	15.01	0.41	0.43	-3.02	-68.40	3.5
		0.09	0.88	-2.22	93.81	-2.8
		0.16	0.25	0.68	-77.84	3.7
		0.09	0.70	-0.54	81.82	-3.8
Ox1_34	13.21	0.30	0.54	1.88	-73.47	3.6
		0.25	0.64	1.91	-80.28	3.8
		0.14	0.47	-0.78	72.27	-3.6
		0.17	0.38	1.88	54.95	-3.2
Ox_12	29.44	0.39	0.18	2.50	55.83	-3.3
		0.19	0.31	-0.97	79.79	-3.7
		0.24	0.37	1.27	-75.55	3.6
		0.23	0.83	1.87	-79.82	3.8
Ox_13	0.00	0.35	0.91	2.52	75.28	-3.7
		0.31	0.56	-1.20	-98.77	4.0
		0.21	0.96	0.96	76.45	-3.6
		0.10	0.72	-0.89	-78.19	3.8
Ox_14	6.40	0.39	0.05	2.93	51.16	-3.4
		0.34	0.11	-1.00	-97.51	4.0
		0.10	0.32	0.36	-70.15	3.6

		0.10	0.54	-1.16	67.04	-3.8
Ox_23	28.86	0.22	0.15	1.80	-66.19	3.8
		0.24	0.27	-1.45	91.96	-3.9
		0.30	0.30	3.09	39.08	-3.1
		0.15	0.26	-1.32	-67.67	3.8
Ox_24	12.74	0.34	0.83	2.51	-78.17	3.7
		0.34	0.48	2.28	58.10	-2.8
		0.23	0.43	0.89	-77.32	3.7
		0.11	0.95	-0.95	79.48	-3.8
Ox2_34	7.98	0.15	0.70	1.48	-72.77	3.8
		0.34	0.48	-1.24	-97.21	4.0
		0.24	0.53	1.84	72.75	-3.6
		0.25	0.97	2.28	71.93	-3.7

Table S13. Spectroscopic data calculated for all BS-species of the reduced $[4Fe\text{-}3S]^{3+}$ model cluster using the B3LYP functional. Energy differences (ΔE) are given in kcal/mol with respect to the lowest energy species. Isomer shifts (δ) and quadrupole splittings (ΔE_Q) are given in mms^{-1} units. The asymmetry parameter (η) is unitless, whereas the isotropic hyperfine coupling (A_{iso}) values are presented in MHz units.

species	ΔE	δ	η	ΔE_Q	A_{iso}	spin pop.
Red1_12	0.00	0.40	0.59	2.82	62.95	-3.5
		0.50	0.40	2.95	65.46	-3.4
		0.23	0.94	-0.64	-67.87	3.6
		0.36	0.17	2.08	-81.17	3.8
Red1_13	18.41	0.45	0.61	2.79	57.51	-3.3
		0.16	0.44	-1.05	-64.48	3.7
		0.35	0.66	2.58	54.72	-3.4
		0.51	0.36	3.41	-49.98	3.5
Red1_14	9.00	0.37	0.30	3.14	41.96	-3.3
		0.32	0.53	1.76	-72.51	3.6
		0.26	0.86	1.17	-68.96	3.6
		0.49	0.36	3.37	46.27	-3.5
Red1_23	12.89	0.44	0.36	2.97	-45.92	3.4
		0.43	0.60	3.50	55.57	-3.5
		0.42	0.58	-2.93	45.68	-3.2
		0.17	0.45	0.93	-77.11	3.9
Red1_24	3.51	0.34	0.71	2.37	-72.56	3.6
		0.39	0.48	-2.75	44.76	-3.3

		0.24	0.28	0.99	-73.71	3.6
		0.49	0.40	2.59	61.44	-3.5
Red1_34	7.04	0.54	0.98	-2.49	-59.12	3.6
		0.25	0.27	-0.95	-77.34	3.7
		0.40	0.52	3.02	43.13	-3.2
		0.50	0.39	3.55	67.72	-3.6
Red2_12	13.27	0.46	0.57	3.28	58.24	-3.5
		0.44	0.70	3.02	61.78	-3.4
		0.20	0.28	-0.82	-72.77	3.6
		0.42	0.69	3.25	-71.65	3.7
Red2_13	12.93	0.70	0.68	3.03	62.77	-3.5
		0.16	0.91	0.99	-70.00	3.8
		0.37	0.44	2.96	53.66	-3.4
		0.51	0.34	3.35	-41.82	3.5
Red2_14	0.00	0.39	0.83	2.89	44.59	-3.3
		0.39	0.79	3.06	-56.96	3.6
		0.19	0.28	0.44	-69.87	3.6
		0.44	0.41	4.08	46.36	-3.5
Red2_23	17.16	0.38	0.52	-1.80	-60.14	3.8
		0.40	0.74	2.76	49.54	-3.2
		0.35	0.72	2.75	58.04	-3.4
		0.50	0.42	2.94	-43.46	3.5
Red2_24	6.11	0.57	0.17	2.21	-76.15	3.7
		0.39	0.77	-2.43	54.47	-3.4
		0.26	0.72	0.90	-70.47	3.6
		0.45	0.65	2.81	43.34	-3.3
Red2_34	10.94	0.55	0.88	2.68	-62.75	3.6
		0.24	0.97	-0.86	-80.47	3.7
		0.40	0.56	3.05	46.81	-3.2
		0.49	0.91	-3.71	69.50	-3.6

Table S14. Spectroscopic data calculated for all BS-species of the semioxidized/semireduced [4Fe-3S]$^{4+}$ model clusterusing the B3LYP functional. Energy differences (ΔE) are given in kcal/mol with respect to the lowest energy species. Isomer shifts (δ) and quadrupole splittings (ΔE_Q) are given in mms^{-1} units. The asymmetry parameter (η) is unitless.

species	ΔE	δ	η	ΔE_Q	spin pop.
Semiox1_12	0.00	0.32	0.75	-0.91	3.6
		0.26	0.59	1.06	3.8
		0.31	0.38	-1.07	-3.6
		0.25	0.73	1.00	-3.8

Semiox1_13	5.16	0.37	0.60	-0.95	-3.5
		0.29	0.73	1.18	3.2
		0.27	0.56	-1.05	-3.6
		0.11	0.41	0.96	3.8
Semiox1_14	8.26	0.42	0.77	-0.95	3.4
		0.31	0.58	1.12	-3.7
		0.20	0.27	-1.08	-3.6
		0.12	0.60	1.02	3.8
Semiox2_12	0.00	0.42	0.75	1.09	3.4
		0.35	0.64	0.73	4.0
		0.29	0.32	-0.98	-3.7
		0.31	0.86	1.02	-3.8
Semiox2_13	23.21	0.42	0.93	1.08	-3.5
		0.26	0.66	0.82	4.0
		0.21	0.44	-0.94	-3.8
		0.41	0.67	1.01	3.4
Semiox2_14	16.00	0.44	0.83	1.12	3.4
		0.28	0.69	0.80	-4.0
		0.39	0.45	-0.98	-3.3
		0.17	0.87	1.05	3.8
Semired1_12	0.00	0.49	0.35	1.23	-3.6
		0.20	0.65	0.93	-3.7
		0.18	0.91	0.89	3.6
		0.42	0.15	1.17	3.7
Semired1_13	12.96	0.50	0.38	1.25	-3.7
		0.10	0.49	0.98	3.7
		0.19	0.65	0.90	-3.5
		0.50	0.12	1.14	3.5
Semired1_14	3.97	0.61	0.13	1.23	-3.5
		0.36	0.67	0.98	3.6
		0.17	0.82	0.87	3.6
		0.19	0.75	1.30	-3.8
Semired2_12	0.00	0.32	0.79	1.17	-3.6
		0.21	0.69	1.04	-3.7
		0.19	0.96	-0.94	3.6
		0.37	0.20	1.17	3.7
Semired2_13	12.96	0.35	0.74	1.18	-3.5
		0.13	0.61	1.12	3.7
		0.16	0.88	0.90	-3.6
		0.43	0.27	1.11	3.5
Semired2_14	6.42	0.37	0.67	1.20	-3.3
		0.29	0.67	1.12	3.6
		0.20	0.97	0.88	3.5
		0.16	0.15	1.12	-3.9

Table S15. Anisotropic A-tensors, A_{ii}, obtained from DFT calculations in MHz, and non-diagonal components A'_{kl} given in the proper principal axes system of the calculated electric field gradient tensor, V_{ij} (V_{zz} largest, $0 \le \eta \le 1$; 1 MHz corresponds to an internal field $A/g_N\beta_N = 0.7238$ T)

Super-oxidized proximal $[4Fe\text{-}3S]^{5+}$ cluster

Fe1: A_{ii} = [-44.4, -60.8, -75.8],

$$A'_{kl} = \begin{bmatrix} -60.1 & 4.1 & -1.9 \\ 4.1 & -45.5 & 1.9 \\ -1.9 & 1.9 & -75.4 \end{bmatrix}$$

Fe2: A_{ii} = [-0.4, +57.9, +89.5],

$$A'_{kl} = \begin{bmatrix} 83.1 & 12.7 & 8.8 \\ 12.7 & 62.3 & -6.5 \\ 8.8 & -6.5 & 1.6 \end{bmatrix}$$

Fe3: A_{ii} = [-43.3, -60.4, -70.2],

$$A'_{kl} = \begin{bmatrix} -61.8 & 1.4 & -6.3 \\ 1.4 & -61.3 & 10.2 \\ -6.3 & 10.2 & -50.8 \end{bmatrix}$$

Fe4: A_{ii} = [+45.4, +59.5, +71.9]

$$A'_{kl} = \begin{bmatrix} 66.9 & 5.2 & -5.0 \\ 5.2 & 63.0 & -3.1 \\ -5.0 & -3.1 & 46.7 \end{bmatrix}$$

H_2-reduced proximal $[4Fe\text{-}3S]^{3+}$ cluster

Fe1: A_{ii} = [-46.7, -66.4, -74.1],

$$A'_{kl} = \begin{bmatrix} -73.3 & 2.5 & 1.2 \\ 2.5 & -66.9 & 1.8 \\ 1.2 & 1.8 & -50. \end{bmatrix}$$

Fe2: A_{ii} = [+29.9, +40.1, +61.4]

$$A'_{kl} = \begin{bmatrix} 40.4 & 2.7 & 0.7 \\ 2.7 & 61.0 & 1.5 \\ 0.7 & 1.5 & 30.0 \end{bmatrix}$$

Fe3: A_{ii} = [-42.5, -50.9, -56.9],

$$A'_{kl} = \begin{bmatrix} -50. & 0.8 & -2.3 \\ 0.8 & -56.5 & 1.7 \\ -2.3 & 1.7 & -43.3 \end{bmatrix}$$

Fe4: A_{ii} = [-2.2, +26.2, +55.7]

$$A'_{kl} = \begin{bmatrix} 29.1 & -10.4 & -6.1 \\ -10.4 & 51.5 & -0.1 \\ -6.1 & -0.1 & -0.9 \end{bmatrix}$$

In the main text of this work essentially only the sign of the isotropic part of the calculated A tensor has been used as a measure for the validity of the different BS solutions for the new [4Fe-3S] cluster. This is reliable and decisive since the spin coupling schemes underlying the BS solutions yield different patterns of positive and negative spin density distributions for the different iron sites. Table 3 shows that also the numerical A_{iso} values compare reasonably well with the experimental data, but by far not good (up to ca. 50% deviation). This may be not surprising in view of the difficulties to obtain better than reasonable Fermi-contact contributions for the hyperfine coupling within the DFT approach for mononuclear Fe(II) and Fe(III) systems (see Neese and Petrenko in ref. 6), even without the phenomena of exchange and double-exchange encountered here for FeS clusters. This limitation should hold also for anisotropic contributions to *A*. Nevertheless, the absence of large off-diagonal elements in the *A*' tensors given above show that the principal axes systems of calculated efg and *A* tensors are reasonably close together, as it would be expected when spin dipole contributions are the main source of anisotropy. This is sensible for high-spin Fe(II) and Fe(III) in FeS clusters without much orbital momentum (in ligand-field theory the axes would be then identical). The numerical values of the A_{kl} components however scatter and deviate from experiment similar to the isotropic parts. Therefore we refrained from further interpretation of interesting cases, for instance when large asymmetry parameters of the efg potentially prevent a unique assignment of the sign of the tensor main component, although the different choices would matter in the simulations. Detailed investigations of the magnetic hyperfine coupling in this system must be the subject of future work.

Fig. S8. Computational model for the proximal iron-sulfur cluster of the membrane-bound respiratory [NiFe]-hydrogenase. All amino acids directly interacting with the iron sulfur cluster core [4Fe-3S] plus Glu_{82} are included. The total charge of the super-oxidized species (a) was kept neutral, whereas the reduced species (b) obtained a charge of -2. The side chain residues were kept frozen at the α-carbons during the geometry optimization (marked with *).

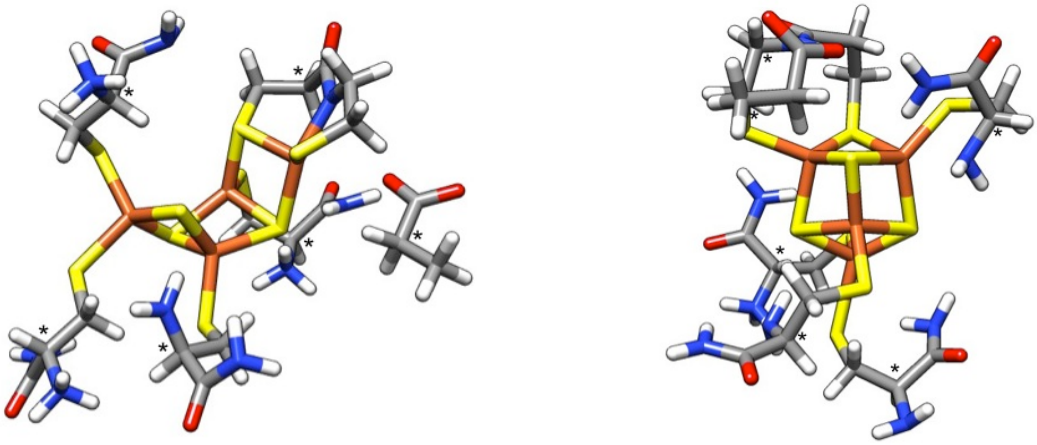

a b

Fig. S9. Weak bonding interactions between iron centers in the model Ox2_24. The delocalized mixed valence pair is formed between Fe1-Fe3. The depicted quasi-restricted orbitals (QROs) are obtained form unrestricted Kohn-Sham orbitals at the B3LYP level of theory. The QROs were localized according to the Pipek-Mezey localization procedure.

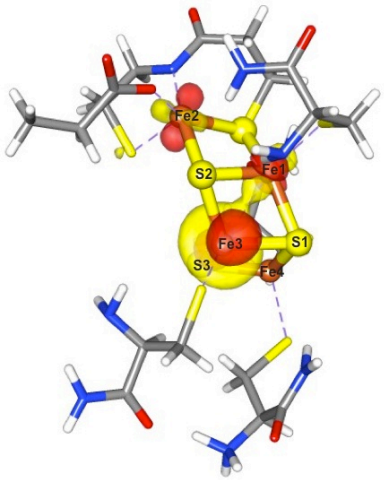

Fig. S10. Spin densities for super-oxidized (a) and reduced (b) models obtained from the B3LYP unrestricted calculations. The yellow isosurface depicts α-density, the red – β-density.

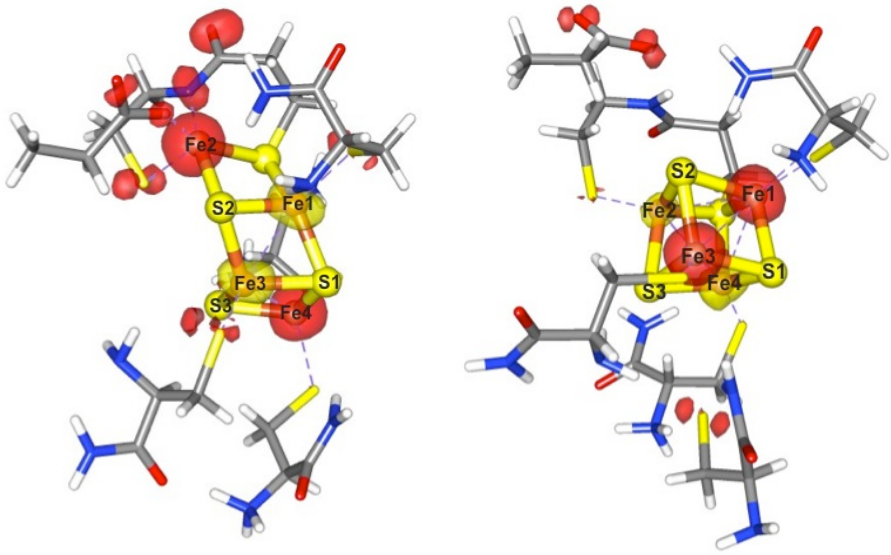

a b

Fig. S11. Calibration of the PBE(a) and B3LYP(b) functionals for the prediction of ^{57}Fe isomer shifts. The calibration procedure includes calculation of the electron density at the nuclei of interest and comparison to the experimentally known isomer shift values. The linear correspondence is then fitted to a straight line using the least squares method. Importantly, to achieve better accuracy in isomer shifts calculations, the "core properties" CP(PPP)[1] basis set was used with the radial integration accuracy parameter increased to 9.0 for iron centers.

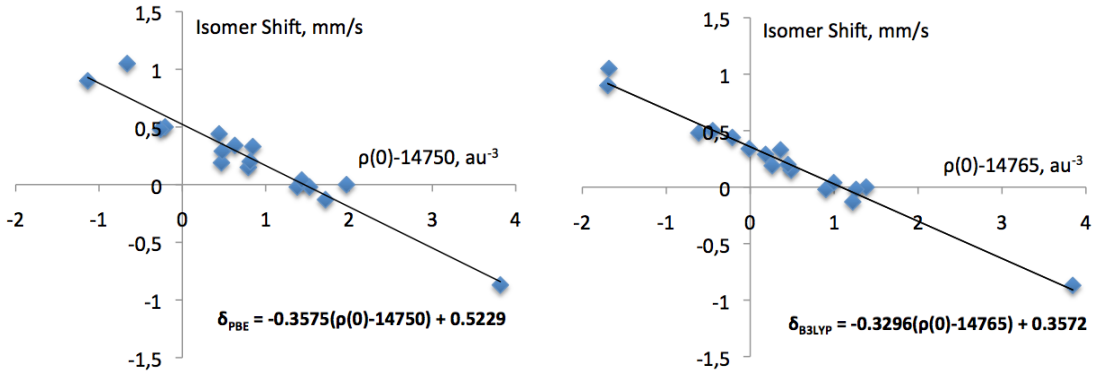

a b

References

(1) Brugna-Guiral M, et al. (2003) [NiFe] hydrogenases from the hyperthermophilic bacterium *Aquifex aeolicus*: properties, function, and phylogenetics*Extremophiles*, **7**: 145.

(2) Kuhn R and Franke W (1935) The redox potential of porphyrexide and porphyrindine. *Berichte der Deutschen Chemischen Gesellschaft* 68: 1528.

(3) Pandelia ME, et al. (2011) Characterization of a unique [FeS] cluster in the electron transfer chain of the oxygen tolerant [NiFe] hydrogenase from *Aquifex aeolicus*. *Proc Natl Acad Sci USA* 108: 6097.

(4) Stoll S and Schweiger A (2006) EasySpin, a comprehensive software package for spectral simulation and analysis in EPR. *J Magn Res* 178: 42.

(5) Bencini A and Gatteschi D (1990) Electron paramagnetic resonance of exchange coupled systems. *Springer Verlag, Berlin*

(6) Gütlich P, Bill E, Trautwein AX (2011) Mössbauer spectroscopy and transition metal chemistry. Fundamentals and applications. *Springer Verlag, Berlin*

(7) Middleton P, et al. (1980) Interpretation of the Mössbauer spectra of the high-potential iron protein from *Chromatium*. *Eur J Biochem* 104: 289.

(8) Volbeda A*, et al.* (2012) X-ray crystallographic and computational studies of the O_2-tolerant [NiFe]-hydrogenase 1 from Escherichia coli. *Proc Natl Acad Sci* 109:5305.

(9) Neese F (2012) The ORCA program system *Wiley Interdiscip. Rev.-Comput. Mol Sci* 2: 73.

(10) Noodleman L (1981) Valence bond description of antiferromagnetic coupling in transition metal dimers *J. Chem. Phys.* 74: 5737.

(11) Noodleman L, Davidson ER (1986) Ligand spin polarization and antiferromagnetic coupling in transition metal dimers*Chem Phys* 109: 131.

(12) Perdew JP, Burke K, Ernzerhof M (1996) Generalized Gradient Approximation Made Simple *Phys Rev Lett* 77: 3865.

(13) Perdew JP, Burke K, Ernzerhof M (1997) Generalized Gradient Approximation Made Simple *Phys Rev Lett* 78: 1396.

(14) Schäfer A, Horn H, Ahlrichs R (1992) Fully optimized contracted Gaussian basis sets for atoms Li to Kr *J Chem Phys* 97: 2571.

(15) Sinnecker S, Rajendran A, Klamt A, Diedenhofen M, Neese F (2006) Calculation of solvent shifts on electronic g-tensors with the conductor-like screening model (COSMO) and its self-consistent generalization to real solvents (direct COSMO-RS) *J Phys Chem A* 110: 2235.

(16) van Wullen C (1998) Molecular density functional calculations in the regular relativistic approximation: Method, application to coinage metal diatomics, hydrides, fluorides and chlorides, and comparison with first-order relativistic calculations *J Chem Phys* 109: 392.

(17) van Lenthe E, Snijders JG, Baerends EJ (1996) The zero-order regular approximation for relativistic effects: The effect of spin–orbit coupling in closed shell molecules *J Chem Phys* 105: 6505.

(18) Schäfer A, Huber C, Ahlrichs R (1994) Fully optimized contracted Gaussian basis sets of triple zeta valence quality for atoms Li to Kr *J Chem Phys* 100: 5829.

(19) Lee CT, Yang WT, Parr RG (1988) Development of the Colle-Salvetti correlation-energy formula into a functional of the electron density*Phys Rev B* 37: 785.

(20) Becke AD (1993) Density-functional thermochemistry. III. The role of exact exchange *J Chem Phys* 98: 5648.

(21) Neese F (2002) Prediction and interpretation of the Fe-57 isomer shift in Mössbauer spectra by density functional theory. *Inorg Chim Acta* 337: 181.

(22) Neese F (2001) Prediction of Electron Paramagnetic Resonance g-values by Coupled Perturbed Hartree-Fock and Kohn-Sham Theory *J Chem Phys* 115: 11080.

(23) Neese F (2005) Efficient and Accurate Approximations to the Molecular Spin-Orbit Coupling Operator and their use in Molecular g-Tensor Calculations *J Chem Phys* 122.

(24) Neese F (2006) mportance of Direct Spin-Spin Coupling and Spin-Flip Excitations for the Zero-Field Splittings of Transition Metal Complexes: A Case Study *J Am Chem Soc* 128: 10213.

(25) Pipek J, Mezey PG (1989) A fast intrinsic localization procedure applicable for ab initio and semiempirical linear combination of atomic orbital wave functions*J Chem Phys* 90: 4916.

(26) Pettersen EF, Goddard TD, Huang CC, Couch GS, Greenblatt DM, Meng EC, Ferrin TE (2004) UCSF Chimera--a visualization system for exploratory research and analysis *J Comput Chem* 25: 1605.

(27) Mayer I (1984) Bond order and valence: Relations to Mulliken's population analysis *Int J Quant Chem* 26: 151.